Fluidised-bed incineration bottom ash as the sole precursor of alkali-activated binders: A comparison with bottom ash from grate incinerators

A. Maldonado-Alameda , J. Mañosa , J. Miro-Escola , A.C. Quintero-Payan , J.M. Chimenos *

Departament de Ciència de Materials i Química Física, Universitat de Barcelona (UB), c. Martí i Franquès 1, 08028 Barcelona, Spain

ARTICLE INFO

ABSTRACT

The novel formulation of alkali-activated binders (AABs) using incineration bottom ash (IBA) from fluidised bed (FB) combustion technology as a sole precursor was assessed. In addition, IBA-FB was compared with IBA from moving grate (IBA-MG) combustion technology. The AABs formulated with IBA-FB (AAB-FB) and IBA-MG (AAB-MG) were also evaluated from a physicochemical, mechanical, and environmental perspective. The results revealed that specific surface area in IBA-FB hinders the retention of kneading water of fresh pastes, affecting the workability, consistency, porosity, and mechanical strength of AAB-FB. Moreover, the low calcium content of IBA-FB requires that the formulated AABs must be cured at higher curing temperatures to ensure the formation of (N,C)ASH gels, while the high calcium content of IBA-MG promotes the formation of CSH gels at room temperature. The compressive strength results demonstrated that AAB-MG ($\approx$ 11 MPa) and AAB-FB ($\approx$ 8 MPa) could be used for non-structural purposes.

1. Introduction

Cement is the most widely used building material worldwide, being ordinary Portland cement (OPC) the most commonly used binder, with a growth in the consumption rate higher than 100% in the last decade [1]. Its high consumption and the thermal processes involved in clinker production have made the OPC one of the primary anthropogenic sources of CO_2 emissions worldwide. Globally, it's estimated that the cement industry generates between 5 and 6% of global CO_2 emissions [2] and consumes 3% of the world's primary energy [3]. Thus, the cement industry must identify alternative binders that require less energy and emits lower greenhouse gas emissions. Alkali-activated binders (AABs) are one of the most promising options due to their high performance and low carbon footprint [4]. Moreover, a wide range of municipal and industrial wastes can be employed as precursors in their formulation [5], promoting the zero-waste principle within the framework of a circular economy and reducing natural resource exploitation.

Bottom ash (IBA) from municipal solid waste incineration (MSWI) stands out as one of the most promising uncommon residual precursors. The potential of IBA as an alkali-activated precursor has been proven in many studies, which revealed the feasibility of formulating alkali-activated IBA binders (AA-IBA) for structural and non-structural

purposes when using IBA as a partial precursor [6–11]. In contrast, the compressive strength is generally lower when IBA is used as the sole precursor [12–14] due to the porosity produced by the presence of metallic aluminium, which reacts with NaOH generating hydrogen gas [15]. However, it is also possible to obtain significant mechanical performances using the most suitable mineralogical and chemical composition fractions, as demonstrated elsewhere [16,17]. In this regard, IBA is an aluminosilicate-rich material composed mainly of non-combustible inorganic substances and combustion ashes. Its composition and physicochemical characteristics depend on the type of incinerators and combustion technology used [18,19].

Three types of combustion technology are currently utilised in waste-to-energy plants, namely, moving grate (MG), fluidised bed (FB) and rotary kiln [20,21]. The first two incineration technologies are mainly intended for the final management of MSW, while the latter is designed for hazardous and other particular types of waste. MG technology is considered extensively proven and is the most used globally, as reported elsewhere [20]. Likewise, FB combustion technology does not reach 5% and 20% in Europe (EU-27) and the United States, respectively. Only China stands out for having approximately 30% of FB incinerators in operation for two main reasons [22]. On the one hand, the investment of FB is generally only 70% of that of MG [23]. Moreover, many provinces

---

in China's eastern, central, and western areas have abundant coals to support MSW combustion [24]. MG incinerators are engineered primarily for the mass feeding of MSW without pre-treatment, requiring minimal pre-processing. Moreover, it maintains operational stability with a wide variation of waste composition and calorific value [25]. After a proper time inside the furnaces for correct combustion, the non-combustible waste fraction falls from the end of the grate into the water trap, where it is cooled via contact with the cooling water. In contrast, FB incinerators only operate with strict feedstock homogeneity and heat value control requirements. As a result, the waste is reduced in size apart from the standard separation and recovery of valuable materials. FB incinerators are usually performed with other waste treatment technologies like mechanical and biological treatment (MBT) [26]. MBT plants are designed to produce a fuel stream known as refuse-derived fuel (RDF). Technology for RDF has been developed to remove bulky and recover non-combustible valuable materials and a large part of the organic fraction to improve combustibility and increase the heat value of waste. For this purpose, trommel screens, air classifiers, optical sorting equipment, magnetic separators and eddy current separators are some of the technological devices frequently found in MBT plants [20]. Furthermore, in the FB incinerator, RDF is suspended in a fluidised bed through inflating air and is burned in a suspension of air and solid-bed material that consists of ash and silica sand. This arrangement allows for uniform heating and high combustion efficiency.

This study aims to compare the potential of IBA from MG (IBA-MG) and FB (IBA-FB) as alkali-activated precursors. The novelty mainly lies in the use of IBA-FB since, to the authors' knowledge, this is the first study that evaluates IBA-FB as the sole precursor in the formulation of AA-IBA binders. Hence, this work provides the opportunity to deepen knowledge about the potential of IBA as an alkali-activated precursor depending on the origin combustion technology. Furthermore, the authors expect that MG and FB combustion technologies lead to different compositions and physicochemical characteristics of IBA, which will influence the final properties and applications of AA-IBA binders. This research is part of a larger project dedicated to studying IBA-MG and its potential application as a precursor [16,17,27–30], where some issues, such as activators' concentration and proportion or precursor-activator ratio, have already been optimised. For the current research, the potential use of IBA-MG and IBA-FB as the sole precursors was assessed by characterising the formulated binder materials from a physicochemical, mechanical, and environmental perspective.

2. Materials and methods

2.1. Materials

Representative samples of IBA from two municipal solid waste incinerators with different combustion technologies were used as a sole precursor in the formulation of AABs. In both cases, the entire fraction of bottom ash was used, as it was collected at the respective facilities.

IBA-MG handled for this research was provided by VECSA, a company responsible for the conditioning and recovery of bottom ash generated by the incineration plant of SIRUSA in Tarragona (Northeast Spain). In this case, the moving grate consists of a rotating drum grate that transports the waste through the furnace. The SIRUSA facility has a capacity of 144 kt of MSW per year, mainly comprised of household rubbish, with a small input from commercial vendors. This facility produces about 32 kt of fresh IBA each year, which is later treated in a conditioning plant (VECSA) where valuable metals are recovered, lightweight unburned materials are removed, and the mineral fraction is sieved to obtain a grading envelope (0–30 mm). Then, the conditioned IBA is stabilised in the open for 2–3 months under natural weathering. Currently, weathered IBA is used as secondary raw material in the construction and civil engineering fields, mainly as a sub-base of road construction [26].

IBA from FB incinerator (IBA-FB) was supplied by SOGAMA, the Galician Society for the Environment, located in the province of A Coruña (Northwest Spain), which provides waste management and treatment services to the majority of the Galician municipalities. The SOGAMA complex, with a capacity of 900 kt of MSW per year, carries out activities to separate the valuable materials and treat and incinerate the remaining waste. Around 270 kt of RDF per year are burned in the waste-to-energy plant equipped with fluidised bed technology. In addition, the facility produces about 65 kt of dry IBA per year, which is currently landfilled [26].

Both IBA samples (50 kg each) were dried at 105 °C for 24 h, then homogenised and stored. A representative sub-sample of each technology was sieved (using standard sieves: 32, 16, 8, 4, 2, 1, 0.5, 0.125, 0.063 mm) to determine the particle size distribution. Afterwards, a magnet (Nd; 0.485 T) was used over the quartered dry IBA to remove magnetic particles. Subsequently, the samples were crushed and grounded in a RETSCH BB 50 jaw crusher to obtain a particle-size powder below 80 μm. The specific surface area by the BET single point method was measured with a Micrometrics Tristar 3000 porosimeter.

The elemental composition of the powder of each IBA sample was evaluated by X-ray fluorescence (XRF) analysis with a Panalytical Philips PW 2400 sequential X-ray spectrophotometer equipped with Uni-Quant® V5.0 software. Moreover, the mineral and crystalline phases of both IBA samples were determined through a Bragg–Brentano PANalytical X'Pert PRO MPD alpha1 powder diffractometer device with $CuK_{\alpha 1}$ radiation (XRD). Finally, the amorphous content ($W_{amorphous}$) of both IBA samples was estimated through the degree of crystallinity (DOC) method [31], following Eq.1.

$$W_{amorphous} = \left(1 - \frac{Crystalline\ Area}{Crystalline\ Area + Amorphous\ Area} \right) \cdot 100 \qquad (1)$$

The potential availability of reactive phases (SiO_2 and Al_2O_3), was determined through chemical attacks with NaOH solutions (4 M, 6 M, and 8 M), as reported in previous studies by the authors [28]. Thus, 1 g of IBA samples was mixed with 100 mL of each activating solution and stirred for 5 h at 80 °C. The resulting solution was filtered and analysed by inductively coupled plasma optical emission spectrometry (ICP-OES), using PerkinElmer Optima ICP-OES 3200 RL equipment to quantify the Si and Al leached. Fourier-transform infrared spectroscopy by attenuated total reflection (FT-IR ATR) was also used to evaluate the chemical structure (in the range 4000–450 cm^{-1} with a resolution of 4 cm^{-1}) through a Spectrum Two™ Perkin Elmer spectrometer.

2.2. Alkali-activated binder formulation

The activator–precursor (A/P) ratio and curing conditions were established according to the setting, consistency, workability and pourability of AAB-MG reported elsewhere [30]. The alkali activator used in this study was a mixture of a commercial Na_2SiO_3 solution (Scharlab S.L.) with a molar ratio $SiO_2/Na_2O = 3.22$ (26.44 wt% of SiO_2 and 8.21 wt% of Na_2O; $\rho = 1.37$ g·cm^{-3}), and a NaOH solution prepared using NaOH pearls (Labbox Labware S.L.; purity greater than 98%) dissolved in deionized water. The concentration (M) of the NaOH solution was determined from the results of the previous study of SiO_2 and Al_2O_3 availability. Based on previous studies, the $Na_2SiO_3/NaOH$ mass ratio (80/20) remained constant in all formulations [30]. The preparation started by mixing the alkaline activator solution (A) for 2 min. Then, the solid (P) was progressively added to the liquid (alkaline activator) for 2 min at 470 rpm to favour the dissolution of reactive phases. Subsequently, the whole mixture was stirred for 1 min at 760 rpm. The resulting fresh pastes were poured into 25 × 25 × 25 mm³ cubic moulds and sealed in plastic bags. Specimens formulated were subjected to different curing temperatures (room temperature and 70 °C on a stove) for 3 days. After this initial curing period, the specimens were demoulded, and the curing stage continued at room temperature and

ambient relative humidity. Finally, after 28 days of curing, the specimens were measured and weighed, before subsequent testing and analysis to determine their chemical, physical, mechanical, and environmental properties. Nine cubic-shaped specimens were prepared for each formulation.

2.3. Alkali-activated binder characterization

Hydrolytic stability was assessed by placing one of the specimens obtained from each formulation in boiling water for 20 min [32]. A visual evaluation was then carried out to assess the stability and structural cohesion of the specimens, both related to the possible dissolution of some of the binder phases. Finally, after drying to constant weight in a desiccator, the specimens were weighed to determine the mass loss and to quantify the water stability and resistance.

XRD determined the mineral and crystalline phases of cured specimens.. The vibrational energies of the most characteristic bonds of the formulated binders were identified through FT-IR ATR in the range of 4000–500 cm^{-1} with a resolution of 4 cm^{-1}, although the study was focused mainly on the 1250–800 cm^{-1} range, corresponding to the symmetric and asymmetric stretching vibrations of Si-O bonds [33]. The microstructure of AABs formulated using both types of IBA as the sole precursor, was conducted using an optical microscope and a scanning electron microscopy (SEM) device (ESEM FEI Quanta 200).

The compressive strength after 28 days of curing was evaluated, for each formulation, by testing three cubic specimens according to UNE-EN 196–1. An Incotecnic MULTI-R1 was used, equipped with a 20 kN load cell and used to apply a progressive load until fracture (loading rate of 240 kg·s^{-1}). Bulk density was determined following the EN1936:2006 standard.

3. Results and discussion

3.1. Characterization of incineration bottom ashes (IBA)

Fig. 1 shows the particle size distribution (PSD) of both IBA samples. PSD is remarkably different between the two IBA, with the fine fraction being more predominant in IBA-FB than in IBA-MG. The size reduction of IBA from MG incinerators occurs inside the combustion chamber due to thermal shock, the movement of the grate itself or friction between the particles. On the other hand, for the IBA from FB incinerators, the size reduction takes place before entering the combustion furnace to maintain the conditions for suspending the particles in the fluidised bed. Subsequently, these identical particles in the fluidised bed continue to decrease in size due to thermal shock or friction with the rest of the particles in the bed.

The elemental composition of both IBA samples, determined by XRF, is described in Table 1. SiO_2, CaO and Al_2O_3 are the most abundant elements found in both samples. After proper alkaline activation, all of them are necessary for forming different gel precursors (CSH, NASH and/or CASH) of the binder matrix. However, there is a significant difference in the content of these elements between the two samples studied. The SiO_2 content in IBA-MG is mainly due to the presence of primary and secondary glass. In contrast, CaO and Al_2O_3 mostly come from fired ceramics and cementitious materials based on OPC [34]. Nonetheless, during the MSW pre-processing treatment in MBT plants, performed to obtain an RDF before fluidised bed combustion, a large portion of non-combustible materials (container glass, magnetic and non-magnetic metals, some fired ceramics, etc.) are removed. Thus, the content of primary glass, metals and fired ceramics in the IBA-FB should be lower than in the IBA-MG. Consequently, the high SiO_2 content in the IBA-FB should be justified by silica sand from the fluidised bed, while the lower CaO and Al_2O_3 contents are also due to the lower presence of fired ceramics. The low chloride content in the IBA-FB is also worth noting, probably due to the lower content of plastic materials (mainly PVC) in the RDF. Furthermore, the LOI percentage shown by the IBA-FB
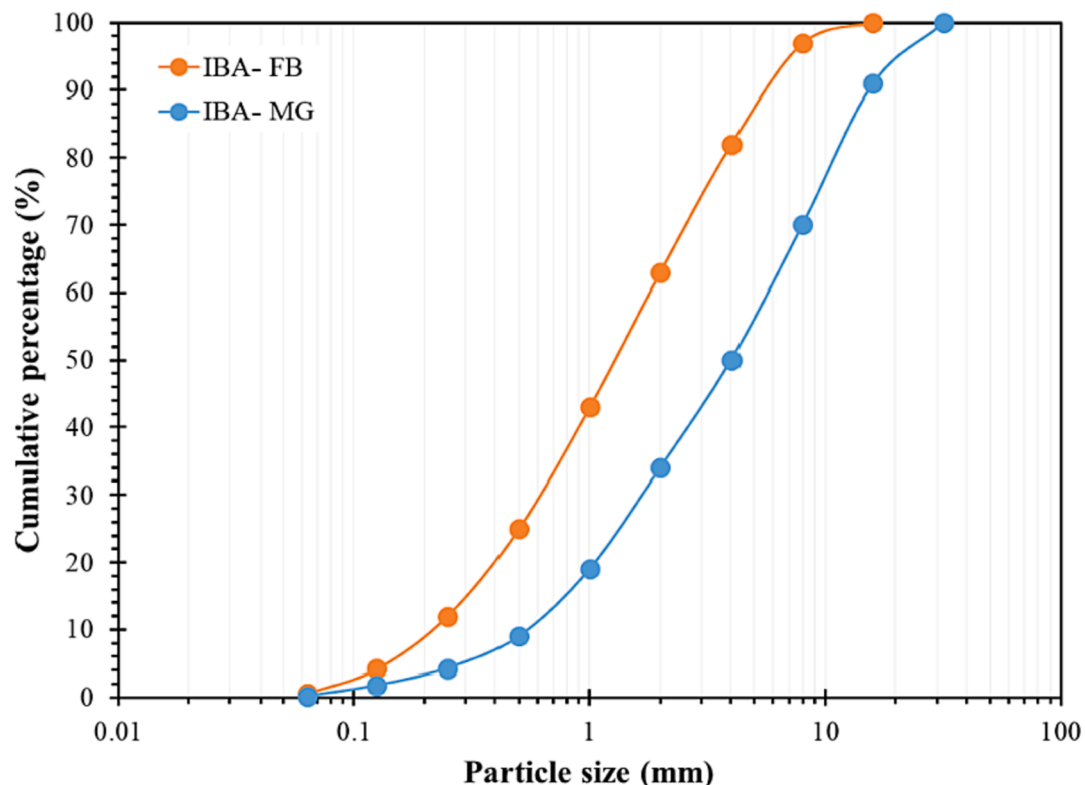

Fig. 1. Particle size distribution of incineration bottom ash (IBA) from a fluidised bed incinerator and a moving grate incinerator.

Table 1

Major elements' composition (wt.%) and specific surface area (BET) of incineration bottom ash (IBA) from a fluidised bed incinerator and a moving grate incinerator.

	IBA-MG	IBA-FB
SiO_2	37.2	64.5
CaO	24.6	14.7
Al_2O_3	9.30	4.97
Na_2O	1.10	1.03
K_2O	1.80	2.45
Fe_2O_3*	8.50	4.31
MgO	1.70	1.17
TiO_2	0.96	0.63
P_2O_5	1.55	1.60
Cl-	1.17	0.23
SO_3	1.74	1.07
[1]LOI	8.75	2.40
BET ($m^2 \cdot g^{-1}$)	5.612	1.823

*The content of iron is expressed as total iron oxide, calculated by stoichiometry from the iron signal, as usually is reported for results from XRF spectrometry analysis.

[1] Loss on ignition at 1000 °C.

sample is lower than the IBA-MG, as a consequence of the lower content of hydroxides and carbonates, generated respectively during tempering of the IBA and outdoors weathering in the case of IBA-MG. Finally, Table 1 also shows the significant difference in results obtained for the specific surface area (BET) between the two IBAs. These values can be explained by the higher content of mineral phases from the thermal decomposition of MSW in the IBA-MG, which subsequently carbonated or oxidized during the weathering process and the higher sand content in the IBA-FG.

Fig. 2 shows X-ray diffraction (XRD) patterns for both IBA samples while Table 2 summarizes the main crystalline phases identified. Only quartz and calcite are found in the two IBA samples. The rest of the crystalline phases are mainly silicates and/or aluminosilicates contained in different fired ceramic materials and aggregates used in construction. Likewise, it should be noted that both IBA samples have an amorphous halo in the 2θ position between 20° and 40°. However, the intensity of

Table 2

The main crystalline and mineral phases of incineration bottom ash (IBA) identified by X-ray diffraction (XRD).

Identified phase		PDF	IBA-MG	IBA-FB
Akermanite	$Ca_2Mg(Si_2O_7)$	01–079-2424	✓	
Microcline	$KAlSi_3O_8$	01–076-0918	✓	
Calcite	$CaCO_3$	01–072-1937	✓	✓
Hematite	Fe_2O_3	01–073-0603		✓
Hydrocalumite	$Ca_4Al_2(OH)_{12}(Cl,CO_3,OH)_2$	01–078-2051	✓	
Magnetite	Fe_3O_4	01–086-1359	✓	
Microcline	$KAlSi_3O_8$	01–076-0918		✓
Quartz	SiO_2	01–078-2315	✓	✓
Wollastonite	$Ca_3(Si_3O_9)$	01–084-0655		✓
Anorthite	$Ca(Al_2Si_2O_8)$	01–086-1706	✓	✓
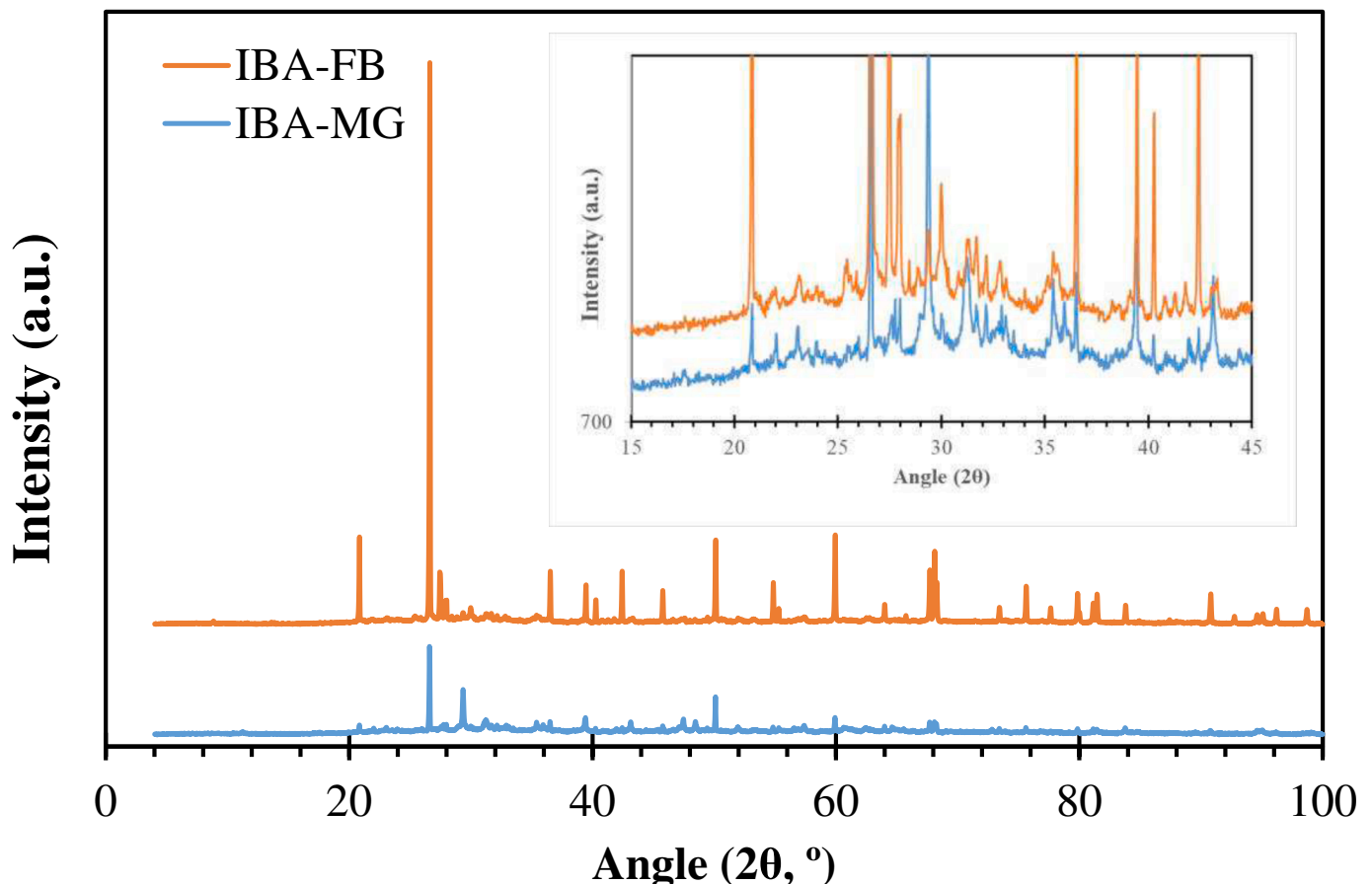
Fig. 2. X-ray diffraction (XRD). Pattern of incineration bottom ash (IBA) from a fluidised bed incinerator and a moving grate incinerator.

the crystalline peaks in the IBA-FB sample is significantly higher than that of the IBA-MG sample, mainly those corresponding to quartz (26.6°) and calcite (36.5°), suggesting a higher crystallinity in IBA-FB than in IBA-MG. Consequently, the amorphous content of IBA-FB and IBA-MG samples, determined by the DOC method, was estimated at 46% and 65%, respectively.

Although the content of mineral phases rich in silicates and aluminosilicates is significant in both IBA samples, given the crystalline nature of these phases and the difference in the amorphous fraction, a notable difference in the availability of SiO_2 and Al_2O_3 to form (N,C)(A)SH gels is expected. It is known that crystalline phases are much less reactive than amorphous phases and that temperature and activator concentration are key factors determining the availability of SiO_2 and Al_2O_3 during the gelation stage [35].

The potential availability of SiO_2 and Al_2O_3, resulting from chemical attacks with different NaOH molarities, is shown in Fig. 3 for both IBA samples. The SiO_2 content in the IBA-FB sample is almost twice than in the IBA-MG (see Table 1). However, the available SiO_2 does not show significant differences between the two bottom ashes (Fig. 2a). Thus, as can be seen in Fig. 2c, the ratio of SiO_2 potentially available to the total SiO_2 determined by XRF (Table 1) is higher for IBA-MG than for IBA-FB. When considering the origin of the SiO_2 in both resources, this finding does not come as a surprise. While the primary source of SiO_2 in IBA-MG is found in the high content of primary and secondary glass (amorphous fraction), in the case of IBA-FB, the SiO_2 content is found mainly in the crystalline phases of the sand and the fired ceramics. Likewise, in the case of IBA-FB, no significant differences were observed when varying the concentration of the alkaline solution since it showed practically the same SiO_2 availability (around 150 g·kg^{-1}). As for the IBA-MG, the highest availability was obtained with the 4 M NaOH solution (around 140 g·kg^{-1}). These differences could be justified by the amount of calcium content in the IBA samples (see Table 1) and its availability to form CSH and CASH gels. The calcium content is mostly related to the crystalline mineral phases of the fired ceramic in IBA-FB. In contrast,

calcium comes mainly from calcite formed during the weathering process for IBA-MG, which could significantly favour the formation of C(A)SH gels.

The potential Al_2O_3 availability between the two IBA samples is considerably different. The availability of Al_2O_3 is higher than 55 g·kg-1 in the worst-case scenario for the IBA-MG (8 M NaOH). In contrast, this availability does not reach 20 g·kg-1 (Fig. 3b) in the best-case scenario for the IBA-FB (6 M NaOH). In this sense, the justification of the potential availability of Al_2O_3 must focus on the distinct aluminium content found in both IBA samples (Table 1) and the main source of this aluminium. The aluminium is mainly related to the mineral phases of the fired clays in IBA-FB. However, in the IBA-MG sample, the metallic aluminium content (e.g. aluminium foil) is significant in fractions below 8 mm, where Eddy currents do not work during the bottom ash conditioning process [34].

FTIR spectra for the two IBA samples are shown in Fig. 4. It should be noted that there are marked differences in the mid-wavenumber region because of the different silica compounds contained in both sample types (see Table 2). In the FTIR spectra for IBA-MG, the band located at 1430 cm^{-1} and the peaks at 875 cm^{-1} and 712 cm^{-1} are ascribed to the stretching and bending modes of O—C—O bonds [36]. This peaks and bands are practically negligible in the IBA-FB sample due to the low content of carbonates.

The FTIR spectrum for the IBA-FB sample contains the most characteristic vibration bands of quartz, which is the main component of the fluidised bed sand: (i) the asymmetric stretching (v_{as}) of Si-O-Si (Q_4) bond at 1161 cm^{-1}, (ii) the asymmetric stretching (v_{as}) of Si-O-Si (Q_3) bond at 1083 cm^{-1}, and (iii) the stretching doublet at 796 cm^{-1} and 777 cm^{-1} [37]. The low presence of quartz content and the higher content of amorphous silica in the IBA-MG sample results in the shift of these bond vibrations to smaller wavenumbers, whose bands overlap at 985 cm^{-1}.

Regarding the environmental performance of the two IBAs used as precursors, as seen in Table 5, they can be classified as non-hazardous materials according to the acceptance limits in landfills stipulated by
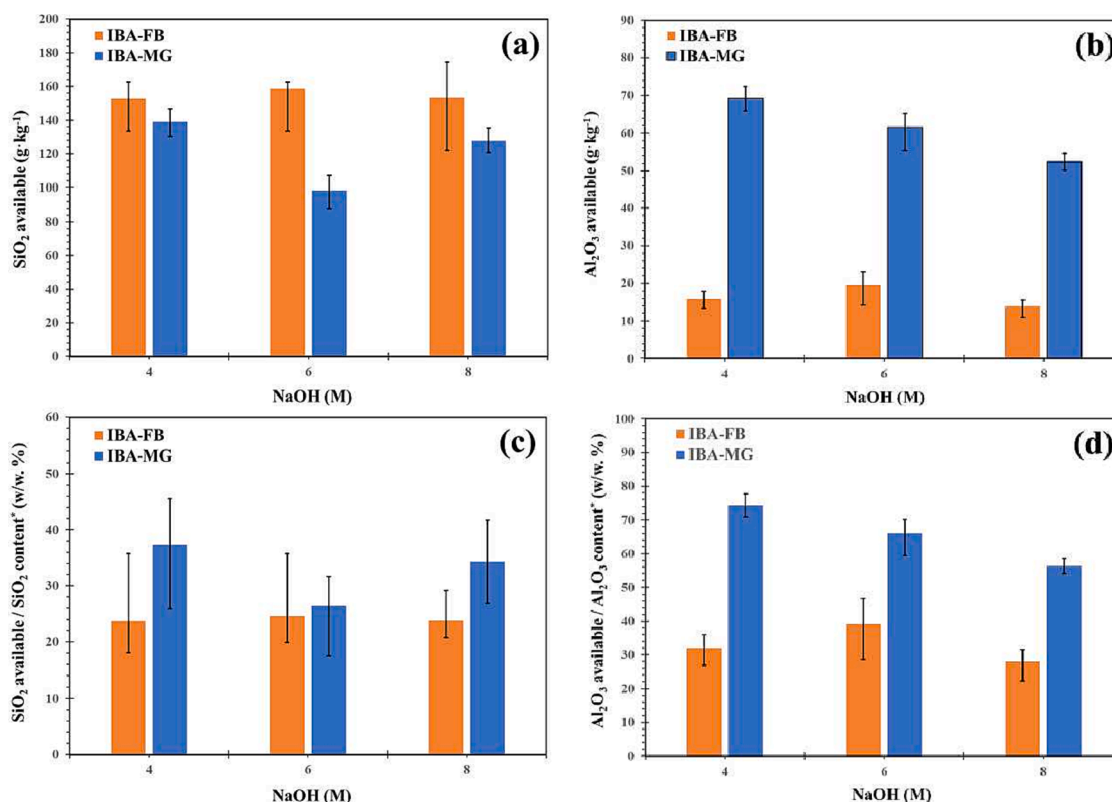

Fig. 3. Availability of (a,c) SiO_2 and (b,d) Al_2O_3 resulting from the chemical attacks. *Results obtained from the XRF analysis (Table 1).
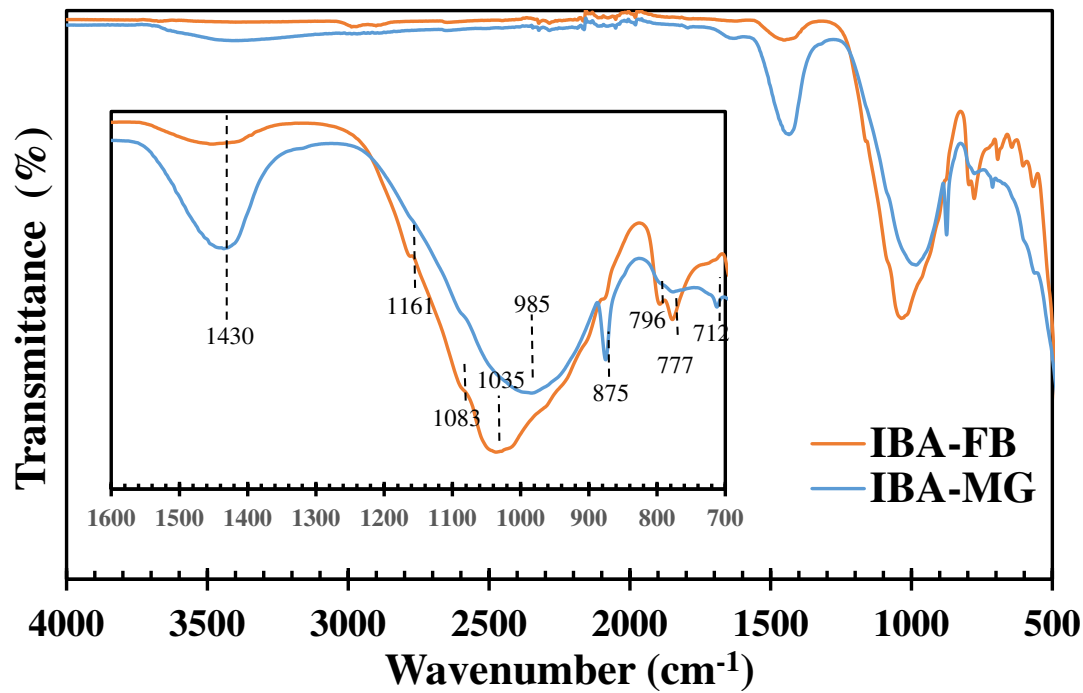
Fig. 4. IBA-MG and IBA-FB FTIR spectra.

the criteria of EU legislation [38]. Nevertheless, it is observed that the leaching of heavy metals and metalloids is slightly lower for the IBA-FB, despite the previous IBA-MG stabilization obtained through a weathering process for its revalorization as secondary aggregate. Therefore, from an environmental perspective, the pre-combustion classification of the valuable materials contained in MSW is more effective than the post-combustion classification of these materials contained in the fresh IBA. During combustion processes, metals and alloys undergo physical and chemical transformations (e.g. oxidation, carbonation, etc.) that promote their subsequent leaching.

3.2. Alkali-activated binder formulation

Table 3 summarizes the performed formulations, the activator/precursor ratio, and the curing temperature of alkali-activated binders obtained using IBA-FB and IBA-MG as the sole precursor. Experimental trials were conducted to determine the optimal range of the A/P ratio in both AA-IBA binders, revealing significant differences in the early curing period (3 days) between both types of IBAs. It is important to note that the optimal activator/precursor ratio in AAB-MG reported in another study by the authors was set at 0.1 [30]. In this sense, for the same A/P ratio, significant differences in the workability and consistency of the poured pastes were observed between the AAB-FB and AAB-MG formulations. Consequently, some of the formulations had to be discarded for two reasons. First, some formulated pastes did not show setting or consistency after 3 days of curing. In contrast, other pastes did not show

Table 3
Mix formulations and curing temperature of alkali-activated binders (AAB) using IBA-FB or IBA-MG as the sole precursor.

	Curing temperature					
	Room temperature (25 ± 2 °C)			(70 ± 1 °C)		
A/P Sample	0.8	1.0		1.2	0.8	1.0	1.2
AAB-FB	✓	*		*	✓	✓	*
AAB-MG	**	✓		✓	**	✓	✓

*Shows no setting or consistency after 3 days of curing.
**Not workable/Not pourable.

suitable workability, which would limit their application in building and civil engineering.

For the same curing temperature, the binders formulated with the IBA of the moving grate incinerator (AAB-MG) require a higher A/P ratio. Thus, it was not possible to obtain specimens with an A/P ratio of 0.8 using IBA-MG as a sole precursor, considering the poor workability and difficulty of pouring the fresh paste into the moulds. In contrast, binders formulated with IBA from the fluidised bed incinerator (AAB-FB) with an A/P ratio greater than 1, after 3 days of curing at room temperature, did not show the setting of fresh paste or consistency that can be demoulded. For an A/P ratio of 1, only with a curing temperature of 70 °C was it possible to obtain AAB-FB specimens with handling consistency. Explanation of the workability, setting and consistency of the fresh pastes must be attributed to differences in calcium content and specific surface area (BET) between the two precursors. A higher calcium content (i.e. IBA-MG) increases the kinetics of the formation of C (A)SH gels, precursors of the cementitious phases, favouring the setting of fresh pastes. Likewise, a greater specific surface area (i.e. IBA-MG) retains a greater quantity of kneading water in the pores of the particles, reducing, as a consequence, the availability of water that facilitates the workability of fresh paste. On the other hand, it is worth noting that an excess of kneading water hinders the setting of fresh pastes and the consistency of binder material.

3.3. Characterization of Alkali-Activated binders (AAB)

No significant differences in hydrolytic stability were observed regardless of the type of IBA used. The specimens of all the tested formulations did not disaggregate and remained cohesive. Weight loss was < 2 wt% in all tested specimens was insufficient to affect the structural consistency. This fact indicates that the consistency of the specimens is due to the alkaline activation of the IBA (FB and MG) and not to the dry water glass (Na_2SiO_3) used as an activator, which is soluble in water.

Fig. 5 shows the 2D cross-sectional images of the binder specimens formulated using both types of IBA with the same A/P ratio and curing temperature, obtained by optical and scanning electron microscopy. In this case, only one formulation for each of the two types of IBA used (i.e.
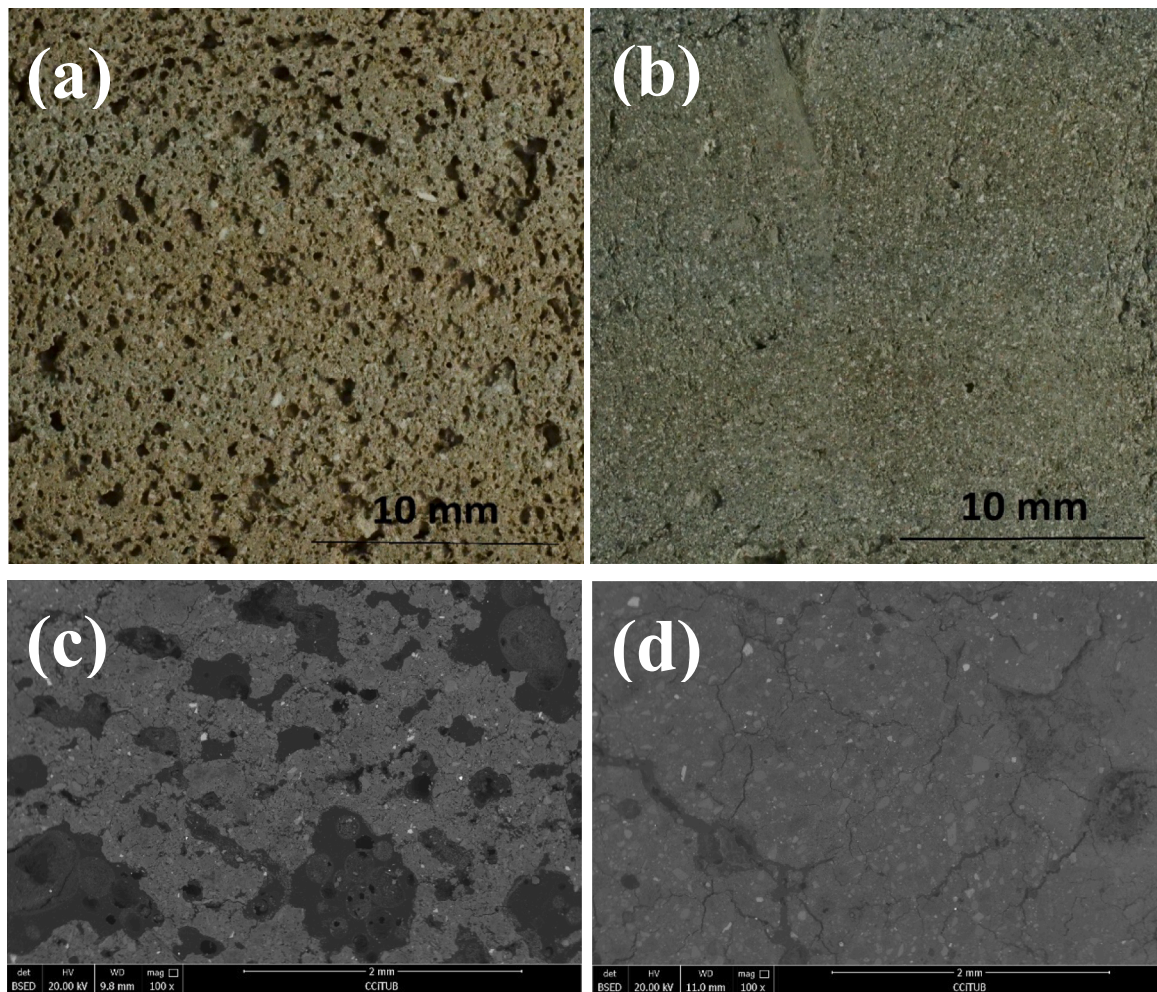
Fig. 5. Micrographs obtained by optical microscopy and scanning electron microscopy of alkali-activated binders formulated with IBA as the sole precursor. (a,c) AAB-FB-70-1.0 and (b,d) AAB-MG-70–1.0.

FB and MG) could be obtained under the same curing conditions: AAB-FB-70–1.0 and AAB-MG-70–1.0 (see Table 3). The resulting images were digitized, and the intensity threshold was enhanced to distinguish the pore (black colour) and the solid matrix of the binder (brownish or grey colour). It can be observed how in addition to the pores and the binder matrix, mineral phases embedded in the matrix are also noticeable. These low reactive mineral phases remain almost unchanged, acting as fine aggregates, and provide increased cohesion and mechanical strength. Therefore, the formulated binder materials can be considered micro-mortar-like materials consisting of cementitious phases and homogeneously distributed fillers throughout the binder matrix. Regarding the porosity, for the same curing conditions, a large difference can be observed between the binder of IBA-FB (Fig. 5a,c) and the one formulated with IBA-MG (Fig. 5b,d). Thus, while the specimens formulated with IBA-MG show higher compactness, the specimens formulated with their counterpart (IBA-FB) show a higher porosity. An increase of the finer fraction (e.g. FB vs MG) increases the effective porosity and the water absorption rate due to the increase of the permeability and sorptivity coefficient of the precursors [39]. As is well known, even at low temperatures, some of the kneading water

Table 4

The main crystalline and mineral phases, identified by XRD, of alkali-activated binders formulated using IBA as the sole precursor.

Identified phase		PDF	AAB-MG				AAB-FB		
			25–1.0	25–1.2	70–1.0	70–1.2	25–0.8	70–0.8	70–1.0
Quartz	SiO_2	01–078-2315	✓	✓	✓	✓	✓	✓	✓
Calcite	$CaCO_3$	01–072-1937	✓	✓	✓	✓			
Albite	$NaAlSi_3O_8$	01–076-0927			✓	✓		✓	✓
Trona	$Na_2CO_3 \cdot NaHCO_3 \cdot 2H_2O$	01–078-1064			✓	✓	✓	✓	✓
Gaylussite	$Na_2Ca(CO_3)_2 \cdot 5H_2O$	01–074-1235	✓	✓	✓	✓			
Kanemite	$HNaSi_2O_5 \cdot 3H_2O$	00–025-1309	✓	✓			✓	✓	✓
Wollastonite	$Ca_3(Si_3O_9)$	01–084-0655					✓		✓
Calcium silicate hydroxide	$Ca_6Si_6O_{17}(OH)_2$	00–015-0313							✓
Calcium silicate hydrate	$3CaO \cdot 2SiO_2 \cdot 4H_2O$ (CSH)	00–011-0507	✓	✓			✓	✓	
Anorthite	$Ca(Al_2Si_2O_8)$	01–086-1706	✓	✓	✓	✓			
Gehlenite	$Ca_2Al(AlSi)O_7$	01–079-1726		✓					
Sodium aluminium silicate hydrate	$Na_2O \cdot Al_2O_3 \cdot SiO_2 \cdot xH_2O$	00–044-0052			✓	✓			

evaporates during the curing process, generating porosity. Therefore, increasing the kneading water content in fresh pastes increases their porosity.

Table 4 summarizes the main crystalline phases identified from all AAB formulations carried out using both IBA-MG and IBA-FB as the sole precursor. It should be noted that some of the major crystalline phases identified in both precursors (see Table 3) have also been identified in most of the formulated binders (i.e. quartz, calcite, albite, wollastonite). Other neoformed mineral phases, such as calcium silicate hydrate, calcium silicate hydroxide or gehlenite, as well as albite and sodium aluminium silicate hydrate, are associated with the secondary products formed during the gelation of CSH, C(A)SH and NASH gels respectively [10,40]. It is worth noting that the neoformation of sodium aluminosilicates was mainly identified in specimens cured at high temperatures (i.e. 70 °C), where increased availability of aluminium can be expected and the formation of NASH gels is favoured [41,42]. Finally, it is also

worth mentioning the presence of neoformed carbonate phases (i.e. trona and gaylussite), which are the products resulting from the reaction of activating solutions with atmospheric CO_2 [43,44].

Fig. 6 shows the FTIR spectra of the AABs formulated with different A/P ratios and cured at different temperatures. By comparison with the precursors used (IBA-FB and IBA-MG), the spectra were evaluated to verify the formation of the main reaction products and the cementitious phases. The characterisation study mainly focused on the most characteristic peaks associated with O—C—O bonds and the broadband of the mid-wavenumber region (at 1200–800 cm-1), associated with asymmetric stretching vibrations Si-O-T (T = Si, Al). When considering the spectra corresponding to the formulations carried out using IBA-FB (Fig. 6a), it is observed that the intensity of the peak at 1430 cm^{-1}, attributed to the carbonates, increases considerably compared to the peak of the precursor. This increase in intensity can be explained by the formation of sodium carbonates (i.e. trona) resulting from the reaction
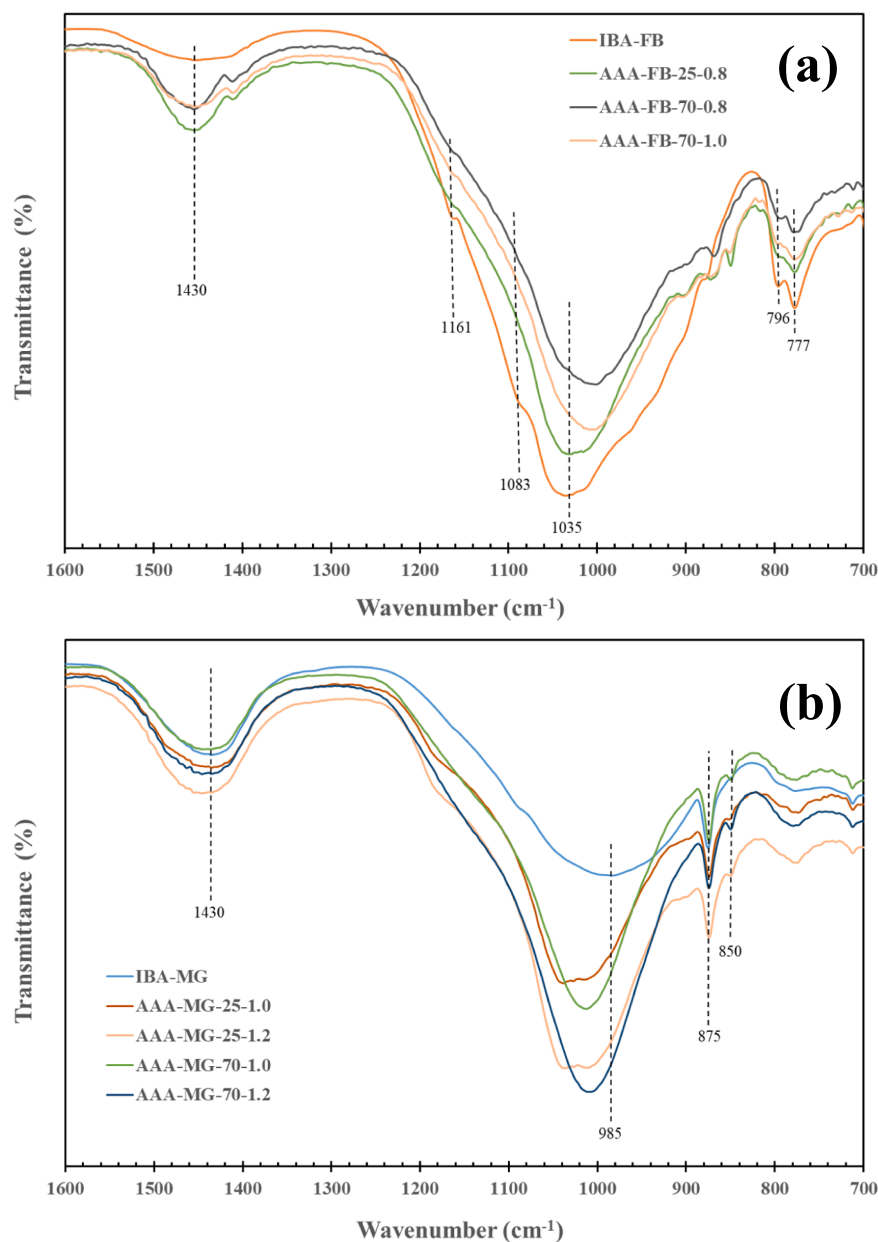

Fig. 6. FTIR spectra of alkali-activated binders using IBA as the sole precursor, formulated with different A/P ratios and cured at different temperatures: (a) AAB-FB and (b) AAB-MG.

of the activator with atmospheric CO_2. This event justifies the appearance of a peak at 875 cm^{-1}, also attributed to the O—C—O bonds of the carbonates. As for the broadband in the mid-wavenumber region (~1035 cm^{-1}), attributed to Si-O-T (T = Si, Al) asymmetric stretching vibrations, a shift towards lower wavenumbers concerning the precursor can be observed in all binders formulated using IBA-FB. The shift of this broad peak is attributed to the formation of new cementitious phases during the gelation stage due to the alkaline activation of the precursor [45]. In addition, a marked decrease in the intensity of the bands at 1161, 1083, 796 and 777 cm-1 is also observed, all associated with the stretching of the Si-O-Si bond. As the curing temperature increases, both the broadband shift and the decrease in the peaks described above become more noticeable. This fact is probably due to the substitution of Si atoms by Al atoms throughout the formation of the (N,C)ASH gels, which causes a band shift to lower wavenumbers because the Al-O bond is longer than the Si-O bond.

Regarding the FTIR spectra of binders formulated using IBA-MG (Fig. 6b), no significant variations and no obvious trend in the intensity of the peaks associated with the O—C—O bonds corresponding to

the carbonates (1430 and 875 cm^{-1}) were observed. The initial presence of high amounts of calcium carbonate in the precursor (IBA-MG) does not allow for observation of any significant variation in the intensity of the peaks due to the neoformation of carbonates (i.e. trona or gaylussite). As for the broadband in the mid-wavenumber region (~985 cm^{-1}), a shift towards higher wavenumbers can be observed because of the formation of CSH gel, which in turn has been a result of the incorporation of calcium from the precursor (IBA-MG) into the lattice of the alkaline-activated silicates. In addition, by comparison to the FTIR spectra of the precursor, the formation of a new peak at 850 cm^{-1} can also be observed, which is associated with the vibration Q^1 of the Si-O bond. This peak can be justified by a greater substitution of Si for Al in the CSH gel, which has generated structures with longer chains [46].

Fig. 7 depicts the compressive strength (σ_c) and bulk density of alkali-activated binders specimens formulated using both types of IBA as the sole precursor. As shown in Fig. 7a, there are significant differences in compressive strength when using IBA-FB or IBA-MG as binder precursors. Comparing the only AAB-MG and AAB-FB samples formulated with the same A/P ratio and curing temperature (i.e. A/P ratio 1.0 and
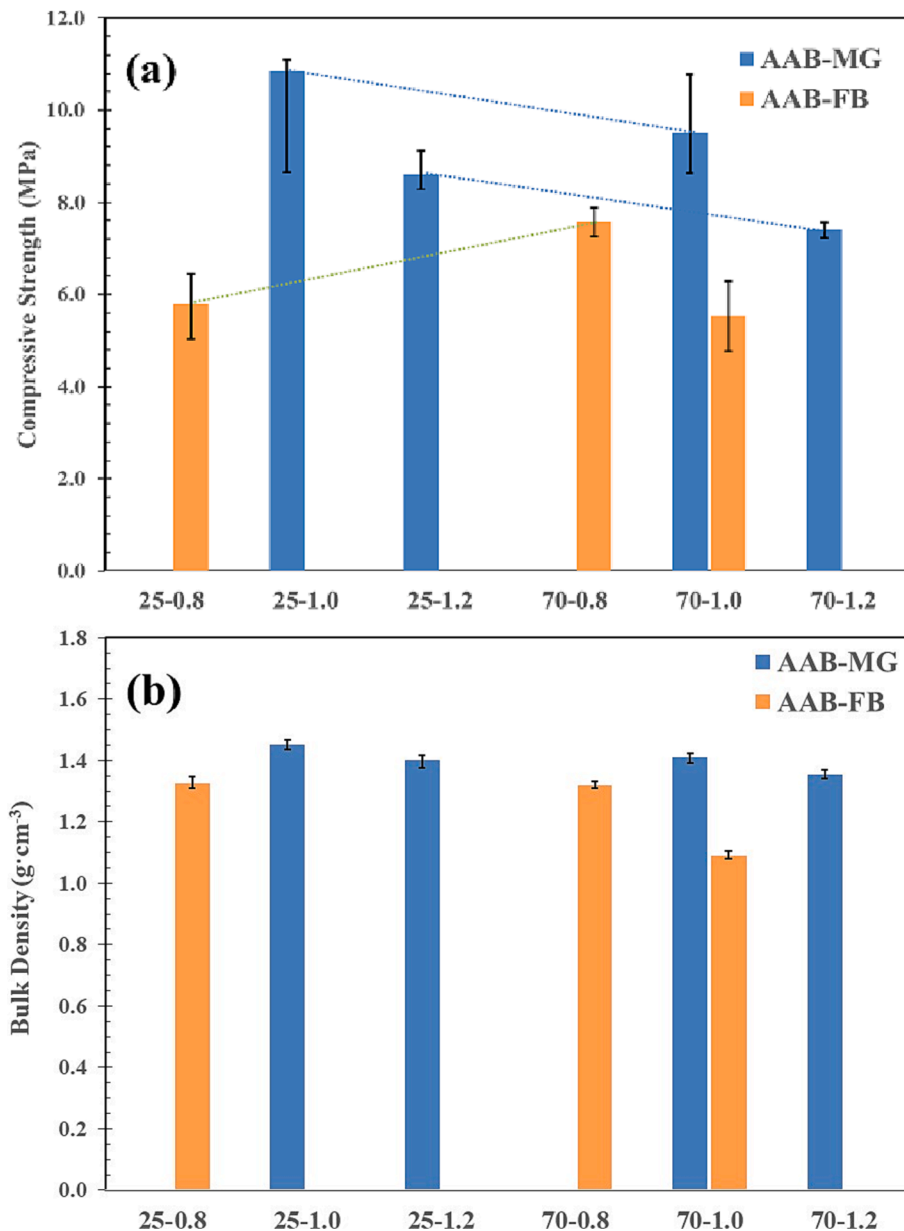

Fig. 7. Compressive strength (σ_c) (a) and bulk density (b) of AAB-FB and AAB-MG specimens at different A/P ratios and curing temperatures.

70 °C of curing temperature), 42% higher compressive strength (4 MPa) has been determined in AAB-MG. This difference can be attributed to the more significant formation of binder phases and the more compact structure of the matrix, as well as its lower porosity (see Fig. 5). In formulations where IBA-MG has been used as the only precursor, it has been determined that, for the same A/P ratio, increasing the curing temperature decreases the compressive strength (dashed trend lines), while for the same curing temperature, increasing the A/P ratio also decreases the compressive strength. This fact can be justified by the nature of the binder phase, mainly composed of CSH which is formed at lower temperatures, and the more compact and cohesive structure of the binder matrix when using less kneading water, respectively. The high content of calcium and glassy phases in IBA-MG facilitates alkaline activation at room temperature. In contrast, for binders formulated with IBA-FB, the highest compressive strengths originated at higher curing temperatures for the same A/P ratio (dashed trend lines), while with an increasing A/P ratio, the compressive resistance decreases for the same curing temperature. In this case, the low reactivity of the aluminosilicates contained in the IBA-FB requires more severe activation conditions, such as increasing the reaction temperature. In addition, it has been determined that the nature of the major binder phase is mainly (N, C)ASH, whose formation kinetics is favoured at high temperatures [42], whereas an increase in kneading water generates greater porosity and less cohesion of the binder matrix with the micro-aggregates embedded.

In terms of bulk density, there are no major differences in the formulations carried out using IBA-MG (Fig. 7b). Only a slight decrease in density is observed with the increase in the A/P ratio and with the increase in the curing temperature, possibly due to a slight increase in porosity. Therefore, the differences in compressive strength determined in these formulations (AAB-MG) must be justified mainly by the amount of neoformed binder phases (mainly CSH), which depend on the availability of the activated aluminosilicates, and by the cohesion of the binder matrix with the embedded micro-aggregates. In contrast, the formulations carried out using IBA-FB as a precursor, a large difference in bulk density was observed when the A/P ratio increased. This fact can be attributed to an increase in porosity when kneading water increases, and it can be thought that its mechanical properties may also be affected accordingly (see Fig. 7a). A slight decrease in the compressive strength can be observed in AAB-MG samples cured at 70 °C. This decrease could likely be due to volumetric variations caused by modifications in the hydration products with the temperature increase [47].

A standard leaching test for granular waste materials (EN 12457–4) was performed to assess the potential environmental impact of the AABs formulated using IBA as the sole precursor, simulating the end of their lifecycle. This test was not intended to assess the potential release of the AAB-IBA during their life service. Table 5 summarizes the leaching concentration of heavy metals and metalloids from both precursors and all tested formulations. As expected, the heavy metals leached from the formulated specimens are higher than those leached from the precursors

as a result of the aggressive attack carried out at the high pH of the alkaline activating solution [27,30,48]. Likewise, as the curing temperature increases, the concentration of metals in the leachate also increases, since the reactivity of the activating solution also increases with temperature. Except for As, the leachate of binders formulated with IBA-MG has a higher concentration of metal(loid)s because the precursor already presents more significant leaching than IBA-FB. However, most metals(loids) remained below the classification of non-hazardous, and only As and Sb exceeded this threshold. Inorganic arsenic has been widely used as copper chromated arsenate for the pressure treatment of lumber, which is essential for its preservation. Although its use in wood is now banned, much of the previously treated lumber ends up in MSW managed in waste-to-energy plants. Arsenic is also used in the electronics and semiconductor industry as gallium arsenide. Treated lumber and electronic components are both difficult to separate in the mechanical and biological treatment processes before combustion in fluidized bed plants. On the other hand, antimony oxide is used as a clarifying or (de)colouring agent in glass manufacturing [38], so its leaching may be mainly due to the high content of glass cullet in MSW, which is in turn higher in IBA-MG.

4. Conclusion

This research revealed the potential of IBA-FB, shedding light on the possibility of using it as an alkali-activated precursor in the formulation of AAB-FB binders instead of traditional Portland cement. Moreover, it was also demonstrated that the physicochemical properties of IBA are highly influenced by the combustion technology used. In this sense, some parameters, such as the specific surface difference and availability of SiO_2, Al_2O_3 and calcium, affect the amount of necessary kneaded water, the fresh pastes' workability or the consistency of samples at the early curing stages. Thus, some AAB-FB and AAB-MG specimens were not obtain depending on the activator/precursor ratio (A/P) and the curing temperature.

From a physicochemical perspective, the AAB-MG and AAB-FB show different trends in binder phase formation (CSH, NASH or (N,C)ASH gels). The high calcium content and the higher availability of SiO_2 in IBA-MG favoured the formation of CSH gels at room temperature. In contrast, the lack of calcium and the lower availability of SiO_2 and Al_2O_3 in IBA-FB requires higher temperatures (e.g. 70 °C) for forming gels (N, C)ASH, as has been demonstrated in the characterisation of binder specimens by FTIR and DRX. In all the formulations, fine homogeneously distributed aggregates were observed, coming from the low reactive mineral phases of the IBA. Therefore, the AAB-MG and AAB-FB can be considered micro-like-mortar, where the cohesion of aggregates and cementitious matrix depends on the kneading water.

The compressive strength results showed better mechanical performance in binder samples formulated with IBA-MG. The formulation with the lowest possible A/P ratio (i.e. A/P = 1.0) and cured at room

Table 5
Leaching concentration (mg·kg^{-1}) in IBA-FB, IBA-MG and alkali-activated binders formulated at different A/P ratios and curing temperatures after the leaching test (EN 12457–4). Curing time: 28 days.

Sample	Hg	Sb	Ba	Cr	Mo	As	Pb	Ni	Zn	Cu	Cd
IBA-FB	<0.01	0.34	0.49	<0.05	0.24	<0.05	<0.05	<0.05	0.21	0.12	<0.01
AAB-FB-25–0.8	<0.01	1.12	0.24	0.17	0.90	2.40	0.09	<0.05	0.27	0.42	<0.01
AAB-FB-70–0.8	<0.01	1.68	0.38	0.14	1.04	4.45	0.09	<0.05	0.36	0.32	<0.01
AAB-FB-70–1.0	<0.01	1.60	0.47	0.13	1.04	4.63	0.20	<0.05	0.36	0.20	<0.01
IBA-MG	<0.01	0.40	0.49	0.13	0.83	<0.05	0.05	<0.05	0.30	1.48	<0.01
AAB-MG-25–1.0	<0.01	1.75	0.06	0.33	1.13	2.01	0.14	0.21	0.76	2.94	<0.01
AAB-MG-25–1.2	<0.01	1.80	0.05	0.41	1.09	1.96	0.12	0.40	0.53	2.64	<0.01
AAB-MG-70–1.0	<0.01	2.30	0.06	0.51	1.60	3.95	0.26	0.17	0.82	3.12	<0.01
AAB-MG-70–1.2	<0.01	2.23	0.14	0.44	1.53	3.67	0.28	0.14	0.93	2.25	<0.01
*Inert waste	0.01	0.06	20	0.5	0.5	0.5	0.5	0.4	4	2	0.04
*Non-hazardous waste	0.2	0.7	100	10	10	2	10	10	50	50	1
*Hazardous waste	2	5	300	70	30	25	50	40	200	100	5

*Limit for acceptance at landfills [38].

temperature presented the best compressive strength (≈ 11 MPa). Under these conditions and given the higher availability of SiO_2 and calcium content, the formation of CSH gels is promoted. The density of AAB-MG slightly decreased when the curing temperature and the A/P ratio increased. This fact is due to an increase in porosity, which also leads to low mechanical performance. In contrast, the best compressive strengths of the AAB-FB occurred at high curing temperatures (i.e. 70 °C) where the activation of SiO_2 and Al_2O_3 is favoured, promoting the formation of (N,C)ASH gels.

Finally, the environmental characterisation simulating the end-of-life scenario of AA-IBA binders revealed that alkaline activation increases the leaching of metals(loid)s concerning the initial precursors (IBA-FB and IBA-MG). Nevertheless, all heavy metal(loid)s are below the limits established for classification as non-hazardous waste for landfill management, except for As and Sb.

Funding

CRediT authorship contribution statement

A. Maldonado-Alameda: Investigation, Methodology, Validation, Writing – review & editing. **J. Mañosa:** Validation, Writing – review & editing. **J. Miro-Escola:** Investigation, Formal analysis. **A.C. Quintero-Payan:** Validation, Writing – review & editing. **J.M. Chimenos:** Conceptualization, Supervision, Writing – original draft, Funding acquisition.

Declaration of Competing Interest

The authors declare that they have no known competing financial interests or personal relationships that could have appeared to influence the work reported in this paper.

Data availability

Data will be made available on request.

Acknowledgements

References

[1] M.J. Quina, E. Bontempi, A. Bogush, S. Schlumberger, G. Weibel, R. Braga, V. Funari, J. Hyks, E. Rasmussen, J. Lederer, Technologies for the management of MSW incineration ashes from gas cleaning: New perspectives on recovery of secondary raw materials and circular economy, Sci. Total Environ. 635 (2018) 526–542, https://doi.org/10.1016/j.scitotenv.2018.04.150.

[2] M. Koushkbaghi, P. Alipour, B. Tahmouresi, E. Mohseni, A. Saradar, P.K. Sarker, Influence of different monomer ratios and recycled concrete aggregate on mechanical properties and durability of geopolymer concretes, Constr. Build. Mater. 205 (2019) 519–528, https://doi.org/10.1016/j.conbuildmat.2019.01.174.

[3] R.M. Andrew, Global CO2 emissions from cement production, Earth Syst. Sci. Data. 10 (2018) 195–217, https://doi.org/10.5194/essd-10-195-2018.

[4] J.L. Provis, Alkali-activated materials, Cem. Concr. Res. 114 (2018) 40–48, https://doi.org/10.1016/j.cemconres.2017.02.009.

[5] S.A. Bernal, E.D. Rodríguez, A.P. Kirchheim, J.L. Provis, Management and valorisation of wastes through use in producing alkali-activated cement materials, J. Chem. Technol. Biotechnol. 91 (2016) 2365–2388, https://doi.org/10.1002/jctb.4927.

[6] X. Gao, B. Yuan, Q.L. Yu, H.J.H. Brouwers, Characterization and application of municipal solid waste incineration (MSWI) bottom ash and waste granite powder in alkali activated slag, J. Clean. Prod. 164 (2017) 410–419, https://doi.org/10.1016/j.jclepro.2017.06.218.

[7] W. Zhu, X. Hong, Y. Liu, E. Yang, Lightweight aerated metakaolin-based geopolymer incorporating municipal solid waste incineration bottom ash as gas-forming agent, J. Clean. Prod. 177 (2018) 775–781, https://doi.org/10.1016/j.jclepro.2017.12.267.

[8] G. Huang, Y. Ji, J. Li, Z. Hou, C. Jin, Use of slaked lime and Portland cement to improve the resistance of MSWI bottom ash-GBFS geopolymer concrete against carbonation, Constr. Build. Mater. 166 (2018) 290–300, https://doi.org/10.1016/j.conbuildmat.2018.01.089.

[9] G. Huang, L. Yuan, Y. Ji, B. Liu, Z. Xu, Cooperative action and compatibility between Portland cement and MSWI bottom ash alkali-activated double gel system materials, Constr. Build. Mater. 209 (2019) 445–453, https://doi.org/10.1016/j.conbuildmat.2019.03.141.

[10] G. Huang, Y. Ji, J. Li, L. Zhang, X. Liu, B. Liu, Effect of activated silica on polymerization mechanism and strength development of MSWI bottom ash alkali-activated mortars, Constr. Build. Mater. 201 (2019) 90–99, https://doi.org/10.1016/j.conbuildmat.2018.12.125.

[11] N. Cristelo, L. Segadães, J. Coelho, B. Chaves, N.R. Sousa, M. de Lurdes Lopes, Recycling municipal solid waste incineration slag and fly ash as precursors in low-range alkaline cements, Waste Manag. 104 (2020) 60–73, https://doi.org/10.1016/j.wasman.2020.01.013.

[12] W. Zhu, X. Chen, L.J. Struble, E.-H. Yang, Feasibility Study of Municipal Solid Waste Incinerator Bottom Ash as Geopolymer Precursor, in: P. Claisse, E. Ganjian, T. Naik (Eds.), Sustain. Constr. Mater. Technol., Coventry University, Coventry, UK, 2016, https://doi.org/10.18552/2016/SCMT4S190.

[13] Z. Chen, Y. Liu, W. Zhu, E.H. Yang, Incinerator bottom ash (IBA) aerated geopolymer, Constr. Build. Mater. 112 (2016) 1025–1031, https://doi.org/10.1016/j.conbuildmat.2016.02.164.

[14] B. Chen, M. Brito van Zijl, A. Keulen, G. Ye, Thermal Treatment on MSWI Bottom Ash for the Utilisation in Alkali Activated Materials, KnE Eng. 2020 (2020) 25–35, https://doi.org/10.18502/keg.v5i4.6792.

[15] J. Liu, Z. Liang, H. Jin, G. Kastiukas, L. Tang, F. Xing, J. Ren, Alkali-activated binders based on incinerator bottom ash combined with limestone-calcined clay or fly ash, Constr. Build. Mater. 320 (2022), 126306, https://doi.org/10.1016/j.conbuildmat.2021.126306.

[16] A. Maldonado-Alameda, J. Giro-Paloma, J. Mañosa, J. Formosa, J.M. Chimenos, Alkali-activated binders based on the coarse fraction of municipal solid waste incineration bottom ash, Bol Soc. Esp. Ceram. Vidr. 61 (2022) 313–324, https://doi.org/10.1016/j.bsecv.2020.12.002.

[17] A. Maldonado-Alameda, J. Giro-Paloma, F. Andreola, L. Barbieri, J.M. Chimenos, I. Lancellotti, Weathered bottom ash from municipal solid waste incineration: Alkaline activation for sustainable binders, Constr. Build. Mater. 327 (2022), 126983, https://doi.org/10.1016/j.conbuildmat.2022.126983.

[18] Z. Youcai, Chapter two - characterization and recycling of bottom ash, Butterworth-Heinemann, 2017, pp. 61–82, https://doi.org/10.1016/B978-0-12-812165-8.00002-0.

[19] M. Šyc, A. Krausová, P. Kameníková, R. Šomplák, M. Pavlas, B. Zach, M. Pohořelý, K. Svoboda, M. Punčochář, Material analysis of Bottom ash from waste-to-energy plants, Waste Manag. 73 (2018) 360–366, https://doi.org/10.1016/j.wasman.2017.10.045.

[20] L. Makarichi, W. Jutidamrongphan, K. Techato, The evolution of waste-to-energy incineration: A review, Renew. Sustain. Energy Rev. 91 (2018) 812–821, https://doi.org/10.1016/j.rser.2018.04.088.

[21] B. Leckner, F. Lind, Combustion of municipal solid waste in fluidized bed or on grate – A comparison, Waste Manag. 109 (2020) 94–108, https://doi.org/10.1016/j.wasman.2020.04.050.

[22] J.-W. Lu, S. Zhang, J. Hai, M. Lei, Status and perspectives of municipal solid waste incineration in China: A comparison with developed regions, Waste Manag. 69 (2017) 170–186, https://doi.org/10.1016/j.wasman.2017.04.014.

[23] D. Chen, T.H. Christensen, Life-cycle assessment (EASEWASTE) of two municipal solid waste incineration technologies in China, Waste Manag. Res. 28 (2010) 508–519, https://doi.org/10.1177/0734242X10361761.

[24] H. Tian, J. Gao, L. Lu, D. Zhao, K. Cheng, P. Qiu, Temporal trends and spatial variation characteristics of hazardous air pollutant emission inventory from municipal solid waste incineration in China, Environ. Sci. Technol. 46 (2012) 10364–10371, https://doi.org/10.1021/es302343s.

[25] G.C. Fitzgerald, 5 - Pre-processing and treatment of municipal solid waste (MSW) prior to incineration, in: N.B. Klinghoffer, M.J.B.T.-W. to, E.C.T. Castaldi (Eds.), Woodhead Publ. Ser. Energy, Woodhead Publishing, 2013, pp. 55–71, doi: https://doi.org/10.1533/9780857096364.2.55.

[26] B.S. Bandara, J.L. Pereira, R.C. Martins, A. Maldonado-Alameda, J.M. Chimenos, M.J. Quina, Opportunities and barriers for valorizing waste incineration bottom ash: Iberian countries as a case study, Appl. Sci. 11 (2021) 9690.

[27] A. Maldonado-Alameda, J. Giro-Paloma, A. Rodríguez-Romero, J. Serret, A. Menargues, A. Andrés, J.M. Chimenos, Environmental potential assessment of MSWI bottom ash-based alkali-activated binders, J. Hazard. Mater. 416 (2021), 125828, https://doi.org/10.1016/j.jhazmat.2021.125828.

[28] A. Maldonado-Alameda, J. Giro-Paloma, A. Svobodova-Sedlackova, J. Formosa, J. M. Chimenos, Municipal solid waste incineration bottom ash as alkali-activated cement precursor depending on particle size, J. Clean. Prod. 242 (2020) 118443.

[29] A. Maldonado-Alameda, J. Mañosa, J. Formosa, J. Giro-Paloma, J.M. Chimenos, Alkali-activated binders using bottom ash from waste-to-energy plants and aluminium recycling waste, Appl. Sci. 11 (2021) 1–15, https://doi.org/10.3390/app11093840.

[30] A. Maldonado-Alameda, J. Giro-Paloma, A. Alfocea-Roig, J. Formosa, J. M. Chimenos, Municipal solid waste incineration bottom ash as sole precursor in the alkali-activated binder formulation, Appl. Sci. 10 (2020) 4129, https://doi.org/10.3390/app10124129.

[31] I.C. Madsen, N.V.Y. Scarlett, A. Kern, Description and survey of methodologies for the determination of amorphous content via X-ray powder diffraction, Zeitschrift Für Krist. 226 (2011) 944–955, https://doi.org/10.1524/zkri.2011.1437.

[32] W. Zhu, X. Chen, L.J. Struble, E.H. Yang, Characterization of calcium-containing phases in alkali-activated municipal solid waste incineration bottom ash binder through chemical extraction and deconvoluted Fourier transform infrared spectra, J. Clean. Prod. 192 (2018) 782–789, https://doi.org/10.1016/j.jclepro.2018.05.049.

[33] Y. Ping, R.J. Kirkpatrick, P. Brent, P.F. McMillan, C. Xiandong, Structure of calcium silicate hydrate (C-S-H): near-, mid-, and far-infrared spectroscopy, J. Am. Ceram. Soc. 82 (1999) 742–748, https://doi.org/10.1111/j.1151-2916.1999.tb01826.x.

[34] R. del Valle-Zermeño, J. Gómez-Manrique, J. Giro-Paloma, J. Formosa, J. M. Chimenos, Material characterization of the MSWI bottom ash as a function of particle size. Effects of glass recycling over time, Sci. Total Environ. 581-582 (2017) 897–905.

[35] C. Ruiz-Santaquiteria, A. Fernándes-Jiménez, A. Palomo, Quantitative determination of reactive SiO2 and Al2O3 in aluminosilicate materials, 13th Int, Congr. Chem. Cem. (2011) 1–7.

[36] M. Criado, A. Palomo, A. Fernández-Jiménez, Alkali activation of fly ashes. Part 1: Effect of curing conditions on the carbonation of the reaction products, Fuel. 84 (2005) 2048–2054, https://doi.org/10.1016/j.fuel.2005.03.030.

[37] A. Autef, E. Joussein, G. Gasgnier, S. Rossignol, Role of the silica source on the geopolymerization rate: A thermal analysis study, J. Non. Cryst. Solids. 366 (2013) 13–21, https://doi.org/10.1016/j.jnoncrysol.2013.01.034.

[38] Council of the European Union, 2003/33/EC, Council Decision establishing criteria and procedures for the acceptance of waste at landfills pursuant to Article 16 of and Annex II to Directive 1999/31/EC, Off. J. Eur. Communities. (2003) 27–49.

[39] V. Revilla-Cuesta, F. Faleschini, M.A. Zanini, M. Skaf, V. Ortega-López, Porosity-based models for estimating the mechanical properties of self-compacting concrete with coarse and fine recycled concrete aggregate, J. Build. Eng. 44 (2021), 103425, https://doi.org/10.1016/j.jobe.2021.103425.

[40] G. Huang, K. Yang, Y. Sun, Z. Lu, X. Zhang, L. Zuo, Y. Feng, R. Qian, Y. Qi, Y. Ji, Z. Xu, Influence of NaOH content on the alkali conversion mechanism in MSWI bottom ash alkali-activated mortars, Constr. Build. Mater. 248 (2020), 118582, https://doi.org/10.1016/j.conbuildmat.2020.118582.

[41] A. Fernández-Jiménez, A. Palomo, Mid-infrared spectroscopic studies of alkali-activated fly ash structure, Microporous Mesoporous Mater. 86 (2005) 207–214, https://doi.org/10.1016/j.micromeso.2005.05.057.

[42] P.C.D. Tortora, A. Maldonado-Alameda, J. Mañosa, A.C. Quintero-Payan, C. Leonelli, I. Lancellotti, J.M. Chimenos, Effect of temperature and humidity on the synthesis of alkali-activated binders based on bottom ash from municipal waste incineration, Sustainability. 14 (2022) 1848, https://doi.org/10.3390/su14031848.

[43] Y. Jun, S.H. Han, J.H. Kim, Early-age strength of CO2 cured alkali-activated blast furnace slag pastes, Constr. Build. Mater. 288 (2021), 123075, https://doi.org/10.1016/j.conbuildmat.2021.123075.

[44] R. Occhipinti, A. Stroscio, C. Finocchiaro, M. Fugazzotto, C. Leonelli, M. José Lo Faro, B. Megna, G. Barone, P. Mazzoleni, Alkali activated materials using pumice from the Aeolian Islands (Sicily, Italy) and their potentiality for cultural heritage applications: Preliminary study, Constr. Build. Mater. 259 (2020), https://doi.org/10.1016/j.conbuildmat.2020.120391.

[45] I. Garcia-Lodeiro, A. Palomo, A. Fernández-Jiménez, D.E. MacPhee, Compatibility studies between N-A-S-H and C-A-S-H gels. Study in the ternary diagram Na2O-CaO-Al2O3-SiO2-H2O, Cem. Concr. Res. 41 (2011) 923–931, https://doi.org/10.1016/j.cemconres.2011.05.006.

[46] D. Torréns-Martín, L. Fernández-Carrasco, S. Martínez-Ramírez, C-S-H gels in blended cements: Study by infrared spectroscopy, (2015).

[47] V. Revilla-Cuesta, M. Skaf, A. Santamaría, A.B. Espinosa, V. Ortega-López, Self-compacting concrete with recycled concrete aggregate subjected to alternating-sign temperature variations: Thermal strain and damage, Case Stud. Constr. Mater. 17 (2022) e01204.

[48] A. Maldonado-Alameda, J. Giro-Paloma, J. Mañosa, J. Formosa, J.M. Chimenos, Alkali-activated binders based on the coarse fraction of municipal solid waste incineration bottom ash, Bol. La Soc. Esp. Ceram. y Vidr. 61 (4) (2022) 313–324.